Science Bulletin 65 (2020) 820–826

Contents lists available at ScienceDirect

Science Bulletin

journal homepage: www.elsevier.com/locate/scib

Science Bulletin
www.scibull.com

Article

Manipulation of surface phonon polaritons in SiC nanorods

Yuehui Li [a,b], Ruishi Qi [a,b], Ruochen Shi [a,b], Ning Li [b], Peng Gao [a,b,c,*]

[a] International Center for Quantum Materials, Peking University, Beijing 100871, China
[b] Electron Microscopy Laboratory, School of Physics, Peking University, Beijing 100871, China
[c] Collaborative Innovation Center of Quantum Matter, Beijing 100871, China

ARTICLE INFO

Article history:
Received 29 November 2019
Received in revised form 10 January 2020
Accepted 11 February 2020
Available online 28 February 2020

Keywords:
Surface phonon polariton
Nanophotonics
Nanostructure
Geometry manipulation
Phononic materials

ABSTRACT

Surface phonon polaritons (SPhPs) are potentially very attractive for subwavelength control and manipulation of light at the infrared to terahertz wavelengths. Probing their propagation behavior in nanostructures is crucial to guide rational device design. Here, aided by monochromatic scanning transmission electron microscopy-electron energy loss spectroscopy technique, we measure the dispersion relation of SPhPs in individual SiC nanorods and reveal the effects of size and shape. We find that the SPhPs can be modulated by the geometric shape and size of SiC nanorods. The energy of SPhPs shows redshift with decreasing radius and the surface optical phonon is mainly concentrated on the surface with large radius. Therefore, the fields can be precisely confined in specific positions by varying the size of the nanorod, allowing effective tuning at nanometer scale. The findings of this work are in agreement with dielectric response theory and numerical simulation, and provide novel strategies for manipulating light in polar dielectrics through shape and size control, enabling the design of novel nanoscale phonon-photonic devices.

1. Introduction

Surface polaritons are electromagnetic surface modes formed by the strong coupling between light and electric or magnetic dipole-carrying excitations, which may result from collective conduction electron oscillations (surface plasmon polaritons, SPPs) or from lattice vibrations in polar crystals (surface phonon polaritons, SPhPs) [1,2]. There are extensive literatures on SPPs approving them to be a promising candidate for nanoscale photonic circuits [3,4]. The shape- and size-dependent SPPs have been well investigated [5,6]. However, the inherent high optical loss of SPPs severely limits their applications. Many recent studies have focused on SPhPs in polar dielectrics, which offer an alternative to achieve low-loss optical devices in the infrared (IR) to terahertz (THz) spectral ranges [7]. The effective wavelength of SPhPs can be up to ten times shorter than the free-space wavelength, thus enabling nanoscale control of light far beyond the diffraction limit [8]. The remarkably small imaginary part of the complex permittivity of phononic materials, compared to plasmonic materials, is advantageous for high Q resonances [9]. Moreover, blackbody emission peaks in the mid-IR range makes the SPhPs a focal point for IR sources, imagers and detectors. Consequently, exploring the behavior of SPhPs in low dimensional systems [8,10,11] and nanomaterials [12–14], to effectively control and manipulate their properties, is of vital importance. Many of the attractive physical properties of SPhPs, including energy transfer [12], spatiotemporal coherent control of lattice vibration [15], and negative index [16] have been previously explored. However, the effect of geometry and size effects, as well as subwavelength light confinement at the nanoscale remains largely unexplored due to challenges associated with experimental detection.

Several vibrational spectroscopy techniques including Raman scattering spectroscopy [17], infrared absorption spectroscopy [18], inelastic neutron scattering [19], inelastic X-ray scattering [20] and high-resolution electron energy loss spectroscopy [21] are limited in spatial resolution, precluding the investigation of size and geometry effects at the nanoscale. Recent work has shown that the spatial resolution of the tip enhanced Raman spectroscopy (TERS) and scanning near-field optical microscopy (SNOM) can be enhanced to ~20 nm, while further improvement is limited by tip-sample contact [22]. To overcome the spatial resolution limit, atomic-wide electron beams have been used to probe localized SPhPs via electron energy loss spectroscopy (EELS) in a scanning transmission electron microscope (STEM) [23–25], which is equipped with a recently-designed monochromator and an ultra-bright cold field emission electron gun [26], providing an electron probe with ~8 meV in energy resolution. This state-of-the-art

* Corresponding author.
E-mail address: p-gao@pku.edu.cn (P. Gao).

https://doi.org/10.1016/j.scib.2020.02.026
2095-9273/

facility allows us to spatially map localized SPhPs in a single nanostructure at the atom level and opens up unprecedented opportunities in this largely unexplored field [26–35].

Here, by combining STEM-EELS and numerical simulations, the propagation, radiation, and dispersion relation of SPhPs are investigated at the 3C-SiC nanorods with various shapes and sizes. We find that the localized SPhPs of nanorods can be strongly affected by geometric shape and size. SPhPs exhibit red-shifts with decreasing the nanorod radius. Furthermore, in nanorods with nonuniform diameter and shape, localized SPhP field can be concentrated on specific positions, demonstrating that localized SPhPs can be effectively controlled and manipulated by tailoring the nanorod geometry. These findings advance our understanding of localized SPhP behavior at the nanoscale and can facilitate superior design for polaritonic applications.

2. Materials and methods

The 3C-SiC nanorod investigated is a commercially available product (XF NANO.INC, China). The SiC nanorod was analytical pure, and the X-ray powder diffraction (XRD) data is shown in Fig. S1 (online). The SiC nanorods were ultrasonicated in alcohol for ~30 min and were dispersed on transmission electron microscope (TEM) sample grids (holy carbon file) to find isolated nanorods. Special pretreatments such as baking the sample under vacuum is used for the removal of possible carbon contamination (Fig. S2 online). EELS data were acquired on a Nion HERMES200 aberration-corrected electron microscope operating at 60 kV. Fig. 1a shows a schematic of EELS operation and Fig. 1b exhibits the diffraction pattern and the first Brillouin zone (hexagon) for zone axis [1 1 0]. Traditional EELS aperture is circle and electrons with all momentum transfers within the circle were collected, lacking momentum information in the integrated spectrum. To obtain momentum-resolved EELS, a slot aperture was used to select the special diffraction direction and obtained the momentum-resolved EELS. In the momentum-resolved experiments, the beam convergence semi-angle was 1.5 mrad and 80 spectra were summed up to obtain a good signal-to-noise ratio. In the Localized SPhPs EELS experiments, the beam convergence semi-angle was 15 mrad and the collection semi-angle was 24.9 mrad with a 1 mm spectrometer entrance aperture. The typical energy resolution (half width of the full zero loss peak, ZLP) was 8 meV for a high signal-to-noise ratio. The probe beam current was ~5–10 pA and the dispersion of per channel was 0.47 meV. The typical dwell time was 100–200 ms to achieve a satisfactory signal-to-noise ratio. Gatan Digital Micrograph software and MATLAB were used to process the data. Atomic-resolved high angle annular dark field (HAADF) images were acquired using Nion HERMES200 microscope with setting the convergence semi-angle 30 mrad. The powder X-ray diffraction data was acquired using Bruker D8 advance X-ray diffractometer.

Due to the instability of the electron beam, the shape of ZLP may slightly change over time. To correct the energy shift of ZLP, the center of ZLP was aligned to zero. To eliminate the effect of beam fluctuation, the aligned spectra were normalized using unsaturated counts of the ZLP. In the loss region, the ZLP forms a background, which was fitted using the power law $I(E) = I_0E^{-r}$ (I_0 and r are adjusted parameters) and was then subtracted [36], as shown in Fig. 1e. Numerical calculations were based on boundary element method (BEM) via the MATLAB MNPBEM Toolbox [37], which incorporates dipole scattering and surface contributions

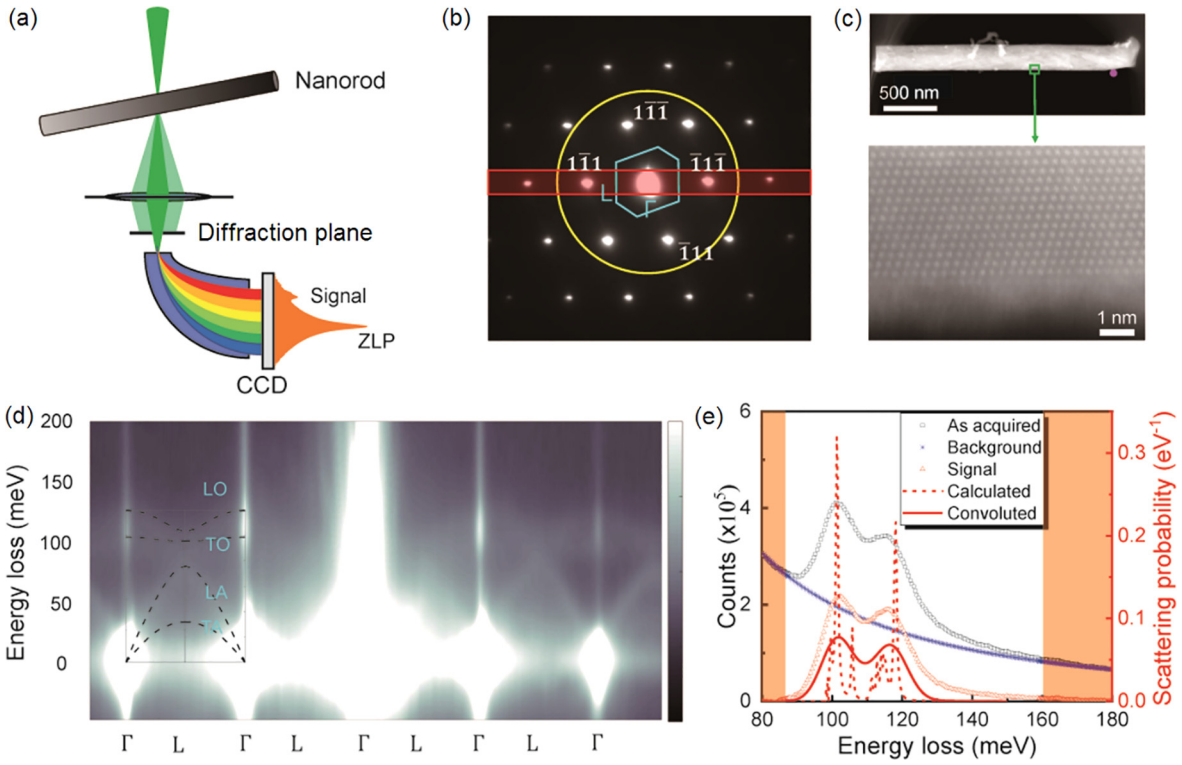

Fig. 1. (Color online) STEM-EELS measurement of localized SPhPs in a SiC nanorod. (a) Schematic diagram of EELS operation. (b) The diffraction pattern and first Brillouin zone for zone axis [1 1 0]. Hexagon: first Brillouin zone. Circle: conventional circle EELS aperture. Rectangle: slot aperture for momentum-resolved EELS measurement. (c) HAADF image showing the morphology and atomic structure of a cubic SiC nanorod viewed from [1 1 0]. (d) Momentum-resolved EELS along the direction ΓLΓLΓ. (e) The typical phonon polariton signal obtained by experiment and simulation. The dash line was the simulated EELS probabilities, containing several resonance modes clearly. The solid line was the calculated spectrum convoluted with a Gaussian function with a width of 10 meV, which accounts for the response function.

that are in good agreement with experiments. The simulations provided insight into localized SPhPs by accounting for surface and shape effects.

The dielectric function of SiC is calculated by the Lorentz oscillator model

$$\varepsilon(\omega)=\varepsilon_{\infty}\left[1+\frac{\omega_{\mathrm{L}}^{2}-\omega_{\mathrm{T}}^{2}}{\omega_{\mathrm{T}}^{2}-\omega^{2}-i\Gamma\omega}\right], \tag{1}$$

where $\varepsilon_{\infty}=6.7$ is the permittivity for high frequencies, $\omega_{\mathrm{T}}=793\ \mathrm{cm}^{-1}$ and $\omega_{\mathrm{L}}=969\ \mathrm{cm}^{-1}$ are the frequency of the transverse optical (TO) phonon and longitudinal optical (LO) phonon, respectively, and $\Gamma=4.76\ \mathrm{cm}^{-1}$ is the damping constant [38].

3. Results and discussion

HAADF images in Fig. 1c show the morphology and atomic structure of a typical cubic SiC nanorod viewed from [1 1 0]. Fig. 1d presents the phonon dispersion measured along the direction ΓLΓLΓ with a slot EELS aperture for zone axis [1 1 0]. The corresponding calculated dispersion line is also shown in the high-order Brillouin zone. The dispersion relation is obtained from the Materials Project (http://www.materialsproject.org) [39] and the phonon band paths are determined by Seek-path developed by Giovanni Pizzi [40]. The calculated dispersion relation is in good agreement with the experimental results in the high-order Brillouin zone, with the exception that TA was not obtained in the experiment. The phonon dispersion was not so clear in the first and second Brillouin zone due to the broadening of the intense central bragg diffraction spot.

It is well known that the Reststrahlen band lies between the TO and LO phonon frequencies, which are identified at the crossover of the real part of dielectric function ($\mathrm{Re}[\varepsilon]=0$). The termination surface breaks the translational symmetry and changes the dielectric environment of the bulk crystal, which leads to the generation of a third resonance [24], such as Fuchs-Kliewer mode (surface optical mode of infinite flat plane, $\mathrm{Re}[\varepsilon]=-1$), Fröhlich mode (surface polariton of sphere, $\mathrm{Re}[\varepsilon]=-2$) and SPhPs. The vibrational frequencies of SPhPs are limited in the Reststrahlen band, where the permittivity is negative. From a dispersion point of view, the phonon polariton is formed due to interactions between the electromagnetic wave induced by the fast electron beam and the TO phonon near Γ. The SPhP dispersion line lies between the transponse optical brach and surface optical (SO) phonon branch.

The SPhPs EELS spectra were recorded in aloof geometry, which means that the electron beam passed near the nanorod but without intersecting it. In this case, the long-range Coulomb field induced by the swift electrons [41–43] excites the localized SPhP modes, and the bulk phonon signal, which is not of interest for this work, is excluded. Fig. 1e displays typical EELS spectrum collected from the circle region in Fig. 1c near a nanorod with a diameter of 240 nm and a length of 2488 nm. The background model used is a power-law function with two-window background fits. The calculated spectrum is convoluted with a Gaussian function with a width of 10 meV, which accounts for the instrument response, is in good agreement with the experimental EELS. In order to demonstrate that the carbon grid has no significant effect, the EELS signal of carbon grid under the same experimental conditions is depicted in Fig. S3 (online) as a reference, and no distinguishable signal was obtained between 80 and 180 meV.

Fig. 2a shows a HAADF image of a SiC nanorod with a radius of 91 nm that is long enough to be seen as semi-infinite, and the spectra were acquired along the dotted line, about 100 nm away from the nanorod surface. Fig. 2b displays the schematic of interference effect. The electron beam is represented as a line current, which induces an electromagnetic field in the sample that reflects off the terminal and acts back on the electron. Standing wave is formed and special wave number $k=\pi/d_{\mathrm{EELS}}$ is selected, where d_{EELS} is the distance between the beam position and the end of the nanorod. In this way, the dispersion of SPhPs in cylinders can be obtained by converting the EELS data from coordinate space to reciprocal space. Fig. 2c depicts the two-dimensional EELS spectra plots. For one branch of the vibrational signal, the energy increases as the electron beam approaches the nanorod terminal, corresponding to the lower interference length d_{EELS} and higher wavevector. The other branch is mainly concentrated in the nanorod terminal. The dispersion relation of the SPhPs (Fig. 2d) of the semi-infinite nanorod in Fig. 2a can be obtained using the relation $k=\pi/d_{\mathrm{EELS}}$. The magenta dotted line, derived from Ref. [44], shows the theoretically predicted dispersion line of an infinite SiC nanorod with the same diameter, which is in excellent agreement with the experiment. As mentioned above, the SPhP resonance energy lies between the TO and SO. The dispersion relation of surface phonon polaritons in an infinite cylinder can be given in the form [44]:

$$v'\varepsilon\alpha-v\varepsilon'\beta=0, \tag{2}$$

where ε (ε') is the dielectric function inside (outside) the cylinder, and

$$v\equiv\left(k^{2}-\varepsilon\omega^{2}/c^{2}\right)^{\frac{1}{2}}, \tag{3}$$

$$v'\equiv\left(k^{2}-\varepsilon'\omega^{2}/c^{2}\right)^{\frac{1}{2}}, \tag{4}$$

$$\alpha\equiv\frac{\mathrm{d}}{\mathrm{d}(va)}\ln I_{0}(va), \tag{5}$$

$$\beta\equiv\frac{\mathrm{d}}{\mathrm{d}(v'a)}\ln K_{0}(v'a), \tag{6}$$

where c is the speed of light in vacuum, a is the radius of cylinder, k is the wavevector, ω is the vibrational frequency, the function I_0 and K_0 are the modified Bessel functions of the first and second kind of order zero. The analytic function only contains the lowest symmetric mode, because the higher modes are immediately damped out due to their very large attenuation factor [45]. The dispersion is dependent upon both the dielectric function and the radius. For the limiting case of the plane interface, $a\to\infty$, $\alpha\to1$, $\beta\to-1$, the surface phonon dispersion relation reduces to

$$v'\varepsilon+v\varepsilon'=0. \tag{7}$$

Fig. 2e shows the spectra acquired in nanorods of different radii r at fixed wave number 0.005 nm^{-1}. There are two resonance peaks, the left one with lower energy and the right one with higher energy (the arrows shown). The lower one is the localized SPhPs mode which concentrated in the nanorod terminal end. The higher one is the SPhPs resonance mode due to the wave interference effects between the beam position and the nanorod terminal end. The SPhP resonance energy red-shifts with decreasing the nanorod radius. So we can obtain the dispersion relation of SPhPs by marking the SPhPs peak positions of every momentum k in Fig. 2d, which is plotted as the triangular scattered points in Fig. 2f. Fig. 2f also shows the dispersion relations of SPhPs for other SiC nanorods with different radii 130 and 218 nm. The lines are computed using the theory [44] and the scatter points are the experimental data. As expected, with increasing r, the dispersion relation converges to infinite flat surface profile (solid line). At larger radius r and larger wave number k, the curve approaches the energy of surface phonon ω_{S}, given by the equation $\varepsilon(\omega_{\mathrm{S}})+1=0$ [46], which is the so-called FK mode [47]. The curve of dispersion

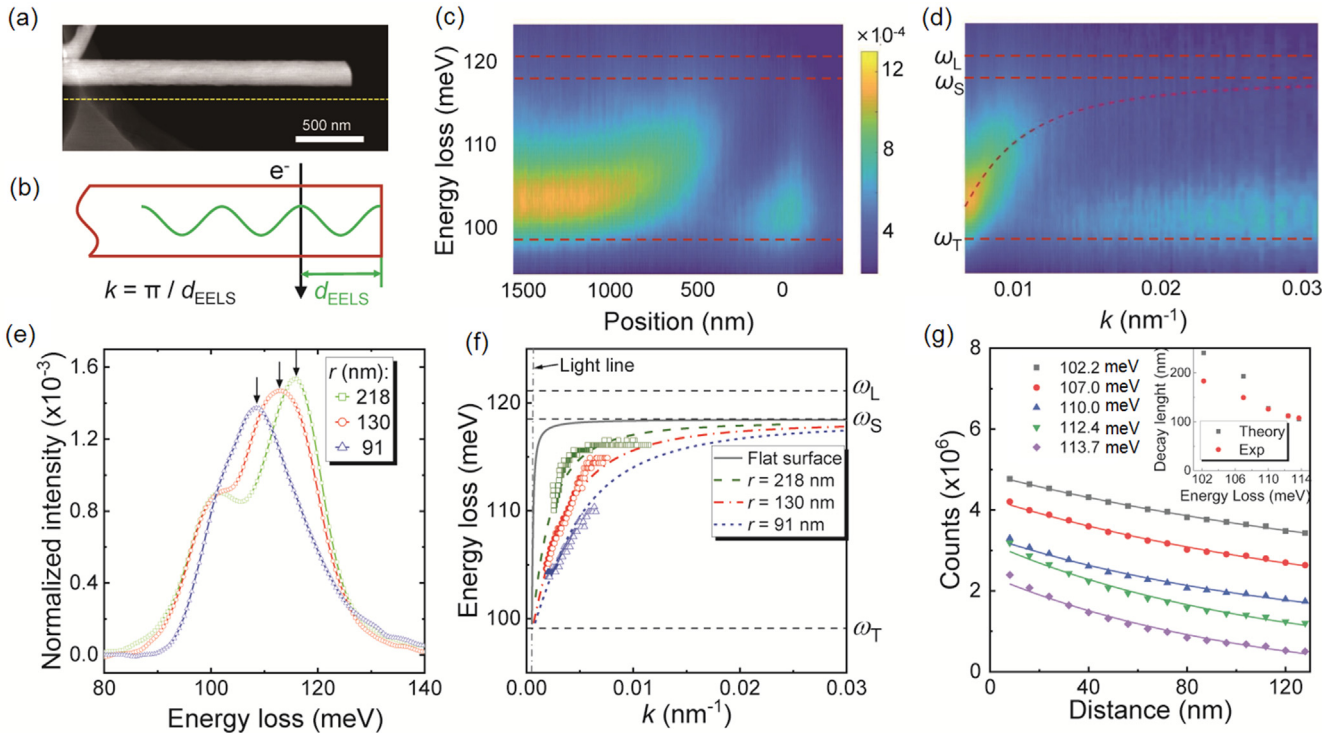

Fig. 2. (Color online) Spatial distribution and dispersion relation. (a) HAADF image for a semi-infinite SiC nanorod, in which the spectra were acquired along the dotted line about 100 nm away from the nanorod surface. (b) Schematic diagram of interference. (c) Two dimensional plots of EELS. (d) Dispersion relation obtained from experiment data. The dotted line is calculated by dielectric theory. (e) EELS signal of different nanorod radii at specific momentum transfer. (f) Dispersion relation of different nanorod radii. The line and scatters are obtained from theory and experiment, respectively. (g) The measured intensity decays exponentially with distance from the nanowire surface. The measured decay lengths of different resonant energy are in good agreement with simulation, as shown in inset.

relation all lies to the right of the light line indicating that the localized SPhPs are nonradiative [48]. At low k, the group velocity of the localized SPhPs, determined by the slope, approaches the speed of light.

As evanescent waves highly localized at the surface, localized SPhP field decays exponentially along the direction perpendicular to the surface. As shown in Fig. 2g, we obtain the signal intensity of different resonance energy to the distance perpendicular to the surface. Then, the data was fitted with an exponential function of the form $I = I_0\exp(-d/\lambda_d)$, where λ_d is the decay length that describes the distance from the edge to the position where the localized SPhP field decreases by a factor of $1/e$, and d is the distance from the nanorod surface. The inset in Fig. 2g displays the decay length of different resonance energy, where the circular (rectangular) scatter is based on the experiment (BEM simulation) data. As the resonance energy increases, the wavevector increases, leading to lower effective wavelength and decay length. The experiment data is in good agreement with the simulation data, except that the decay length of the low order resonances of the simulation is a bit larger than that of the experiment. This discrepancy may be resulted from the contribution of the field of higher resonance energy to the measurement of the lower resonance energy due to the limited energy resolution.

Fig. 3 shows the other two nanorods that have different geometries. Fig. 3a depicts a nanorod which is approximately the combination of a cylinder and a cone. Fig. 3b displays the corresponding two-dimensional plots of normalized intensity. The simulated EEL probabilities of the sample are shown in Fig. 3c, which are convolved with a Gaussian function to account for non-ideal energy resolution. The simulation is in agreement with the experiment. The sharp end on the right side breaks the reflection symmetry, which has a significant effect on the polariton response. Contrary to the normal end in Fig. 2 where SPhPs energy increases while approaching the nanorod end, the polariton energy decreases while approaching the sharp end. We attribute it to the decreasing radius as approaching the sharp end, as shown in Fig. 2f.

Fig. 3d shows a nanorod that looks like two back-to-back sandglasses with the corresponding two-dimensional normalized intensity plot depicted in Fig. 3e. The interference due to the convex-edge reflection gives rise to higher-order resonance modes compared to the center axis, which is similar to the sample above. The smaller radius limits the vibrational energy, as shown in Fig. 2f, leading to lower energies than the adjacent nanorod. Fig. 3f shows the simulated EEL probabilities, that are in good agreement with Fig. 3e. To obtain the space distribution of fixed resonance energy, the EELS spectra around the sample were acquired. The near-field distribution at three resonance energies 99, 106, and 117 meV were presented in Fig. 3g–i, exhibiting significantly different profiles. We have set the bulk intensity to zero to highlight the surface distribution, because the sample was too thick to get any physically meaningful signal from the bulk but some noise, as shown in Fig. S4 (online). At 99 meV, the field amplitude at the nanorod is uniform. No constructuive or destructive interference is observed as it approaches the long wavelength limit. At 106 meV, however, there is constructive interference at the slim part, resulting in an increase in the near-field intensity. At 117 meV, the near-field intensity is high at the convex-edge, which is attribute to the high k value due to the interference between electron source and the convex-edge.

Fig. 4 depicts the simulated EEL probability of different resonance modes surrounding the SiC nanorods, including normal cylinder (Fig. 4a), tip-end (Fig. 4b) and sandglass-like (Fig. 4c). The white dotted lines outline the nanorods. Both the longitudinal modes m = 1–5 and transverse mode of these nanorods are excited

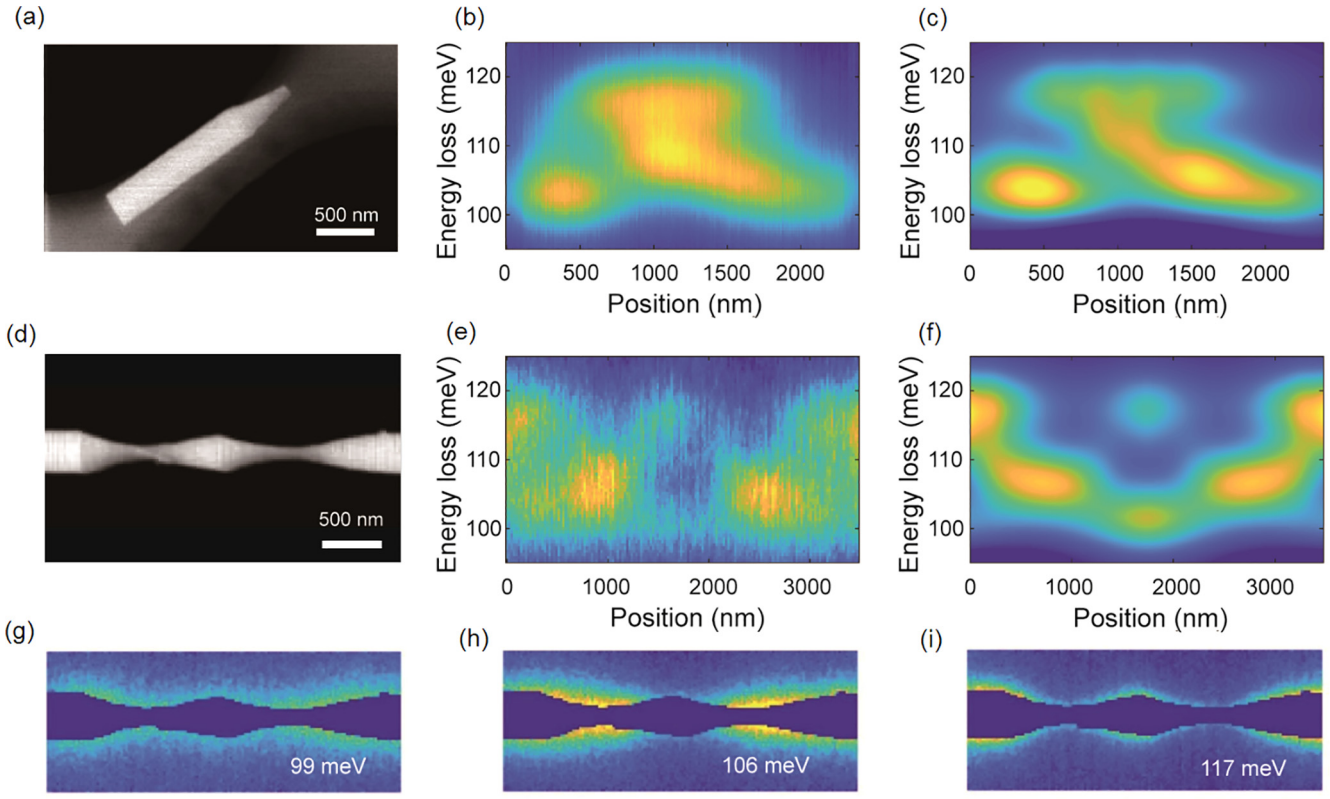

Fig. 3. (Color online) Geometry effects. (a) HAADF image, (b) experimental EELS signal, and (c) simulated EELS of a nanorod with tip-end. The sharp end in (a) directs to the increasing direction of the horizontal axis in (b) and (c). (d) HAADF image, (e) experimental EELS signal, and (f) simulated EELS of a nanorod with back-to-back sandglasses. (g–i) Spatial distribution of intensity associated with different resonance energies.

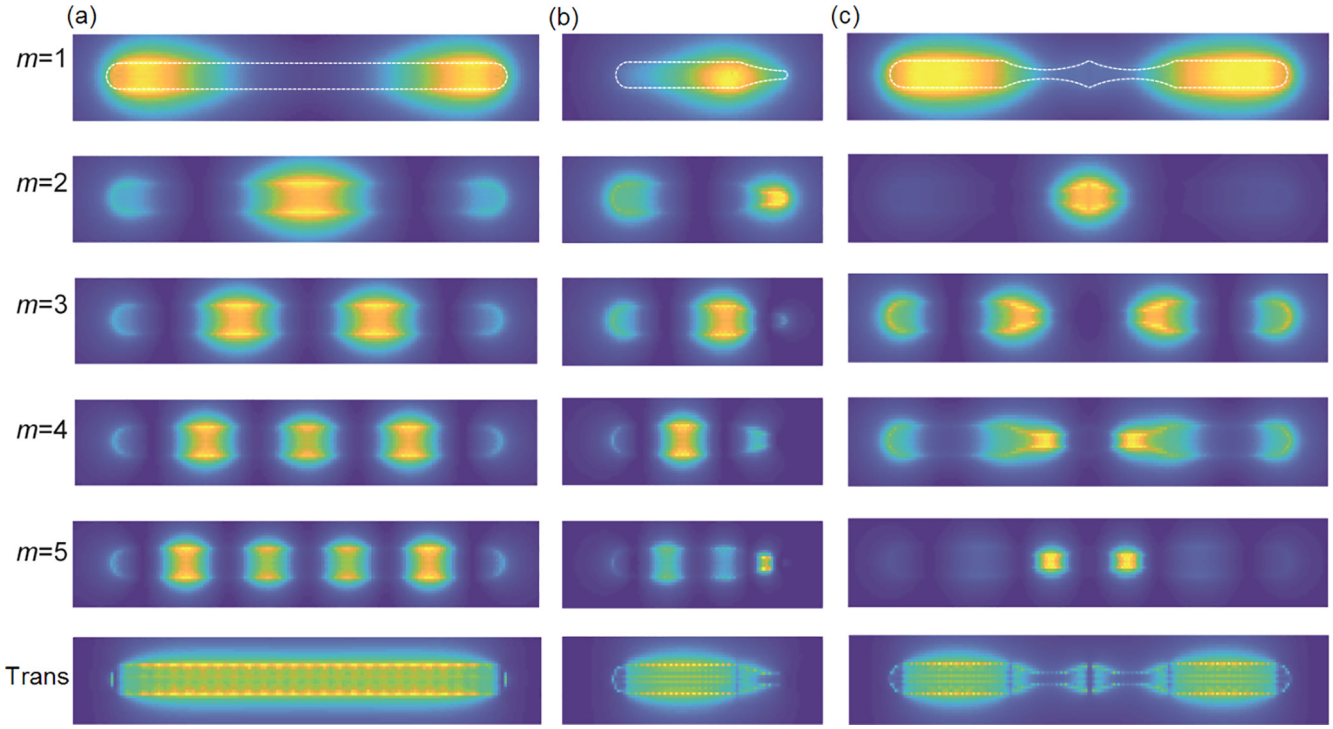

Fig. 4. (Color online) Simulated EEL probabilities surrounding different types of SiC nanorods. (a–c) The simulated EEL probabilities of localized SPhP resonance modes surrounding SiC nanorods, including normal cylinder (a), tip-end (b), and sandglass-like (c). Longitudinal modes m = 1–5 are shown as well as transverse (trans) excitations.

[49], which are significantly different from the optical far-field techniques that can only excite the odd modes due to the selection rules under the quasistatic approximation. STEM-EELS and optical near-field spectroscopies are both related to the electromagnetic local density of states and their maps are similar [13]. The EEL probability distributions of transverse modes are similar, which are concentrated in the nanorod surface and are nearly uniform in the surface except weaker in the rod end because the local fields in the rod end are predominatly perpendicular the electron trajectory [49]. For the longitudinal modes, dipole and multipolar resonances exhibite spatial amplitude modulation. For the nanorod (Fig. 4a), the field of the lowest resonance mode (m = 1) is concentrated at the nanorod ends. On the other hand, for the higher resonance modes, the field of two ends is weaker than that of other anti-nodes with similar intensities due to the perpendicular local fields in the rod ends. For the tip-end (Fig. 4b), the longitudinal resonance modes distribution is not centrosymmetric like nanorod (Fig. 4a) since the tip-end breaks the reflection symmetry. A major difference is that the signal intensity of the lowest resonane mode is concentrated in the interior, not like cylinder (Fig. 4a) and sandglass-like (Fig. 4c) where the lowest resonance modes are concentrated at the nanorod ends. The lowest resonance mode is like a monopole mode due to the broken symmetry. Moreover, the fields are more likely close to the tip end. For the sandglass-like (Fig. 4c), the signal intensity of longitudinal resonance modes is more likely concentrated in the slim part, except for the lowest resonance mode. This is similar to the "hot spot" in SPP, which appears at the point where the translation symmetry is broken [50–52]. We have to note that there are only three nodes for the resonance mode m = 4, normally four nodes, which is not clear yet. This phenomenon may be utilized to concentrate electric field at the subwavelength scale. At present, there are still challenges associated with distinguishing discrete modes due to insufficient energy resolution. We expect significant advances in this field, with the further improvement of STEM-EELS resolution in the future.

4. Conclusions

In summary, we present a systematic study of the relationship between geometric and size properties of individual SiC nanorods and their SPhP resonant properties using STEM-EELS. We demonstrate that electron beam excites localized SPhPs near the sample edge. The SPhP resonance energy red-shifts with decreasing the nanorod diameter. Moreover, our findings show that geometric shape plays a major role in determining the SPhP resonance. We obtain the dispersion relations of SPhPs in STEM-EELS systems by transforming the coordinate space to the reciprocal space. Most importantly, by maping the surface phonon polaritons using electron beam, our work demonstrates that STEM-EELS provides a novel approach to study the localization and dispersion relation of surface phonon polaritons in complex dielectric nanostructures.

Conflict of interest

The authors declare that they have no conflict of interest.

Acknowledgments

We gratefully acknowledge the support from the "2011 Program" Peking-Tsinghua-IOP, China Collaborative Innovation Center of Quantum Matter. The authors acknowledge Electron Microscopy Laboratory of Peking University, China for the use of Cs corrected electron microscope. This work was supported by the National Natural Science Foundation of China (11974023, 51672007), the National Key R&D Program of China (2016YFA0300804), the National Equipment Program of China (ZDYZ2015-1), and the Key-Area Research and Development Program of Guangdong Provience (2018B030327001, 2018B010109009).

Author contributions

Peng Gao conceived the research project. Yuehui Li carried out the experimental measurements. Yuehui Li, Ruishi Qi, Ruochen Shi and Ning Li developed the model and performed the numerical simulations. All the authors contributed to the discussion and the writing of the manuscript.

Appendix A. Supplementary materials

Supplementary materials to this article can be found online at https://doi.org/10.1016/j.scib.2020.02.026.

References

[1] Gupta R, Xiong Q, Mahan GD, et al. Surface optical phonons in gallium phosphide nanowires. Nano Lett 2003;3:1745–50.
[2] Xiong Q, Wang J, Reese O, et al. Raman scattering from surface phonons in rectangular cross-sectional w-ZnS nanowires. Nano Lett 2004;4:1991–6.
[3] Pohl M, Belotelov VI, Akimov IA, et al. Plasmonic crystals for ultrafast nanophotonics: optical switching of surface plasmon polaritons. Phys Rev B 2012;85:081401(R).
[4] Gordon R. Surface plasmon nanophotonics: a tutorial. IEEE Nanotechnol Mag 2008;2:12–8.
[5] Orendorff CJ, Sau TK, Murphy CJ. Shape-dependent plasmon-resonant gold nanoparticles. Small 2006;2:636–9.
[6] Sepúlveda B, Alaverdyan Y, Alegret J, et al. Shape effects in the localized surface plasmon resonance of single nanoholes in thin metal films. Opt Express 2008;16:5609–16.
[7] Caldwell JD, Lindsay L, Giannini V, et al. Low-loss, infrared and terahertz nanophotonics using surface phonon polaritons. Nanophotonics 2015;4:44–68.
[8] Dai S, Fei Z, Ma Q, et al. Tunable phonon polaritons in atomically thin van der Waals crystals of Boron Nitride. Science 2014;343:1125–9.
[9] Qiang B, Dubrovkin AM, Krishnamoorthy HNS, et al. High Q-factor controllable phononic modes in hybrid phononic-dielectric structures. Adv Photonics 2019;1:026001.
[10] Ma W, Alonso-González P, Li S, et al. In-plane anisotropic and ultra-low-loss polaritons in a natural van der Waals crystal. Nature 2018;562:557.
[11] Jung S, Park M, Park J, et al. Vibrational properties of h-BN and h-BN-Graphene heterostructures probed by inelastic electron tunneling spectroscopy. Sci Rep 2015;5:16642.
[12] Renger J, Grafström S, Eng LM, et al. Resonant light scattering by near-field-induced phonon polaritons. Phys Rev B 2005;71:075410.
[13] Lourenço-Martins H, Kociak M. Vibrational surface electron-energy-loss spectroscopy probes sonfined surface-phonon modes. Phys Rev X 2017;7:041059.
[14] Shi C, Beecher AN, Li Y, et al. Size-dependent lattice dynamics of atomically precise cadmium selenide quantum dots. Phys Rev Lett 2019;122:026101.
[15] Feurer T, Vaughan JC, Nelson KA. Spatiotemporal coherent control of lattice vibrational waves. Science 2003;299:374–7.
[16] Shvets G. Photonic approach to making a material with a negative index of refraction. Phys Rev B 2003;67:035109.
[17] Efremov EV, Ariese F, Gooijer C. Achievements in resonance Raman spectroscopy: review of a technique with a distinct analytical chemistry potential. Anal Chim Acta 2008;606:119–34.
[18] Anderson MS. Surface enhanced infrared absorption by coupling phonon and plasma resonance. Appl Phys Lett 2005;87:144102.
[19] Nicklow R, Wakabayashi N, Smith HG. Lattice dynamics of pyrolytic graphite. Phys Rev B 1972;5:4951–62.
[20] Le Tacon M, Bosak A, Souliou SM, et al. Inelastic X-ray scattering in $YBa_2Cu_3O_{6.6}$ reveals giant phonon anomalies and elastic central peak due to charge-density-wave formation. Nat Phys 2014;10:52–8.
[21] Kostov KL, Polzin S, Saha SK, et al. Surface-phonon dispersion of a NiO(100) thin film. Phys Rev B 2013;87:235416.
[22] Jokisaari JR, Hachtel JA, Hu X, et al. Vibrational spectroscopy of water with high spatial resolution. Adv Mater 2018;30:1802702.
[23] Konecná A, Venkatraman K, March K, et al. Vibrational electron energy loss spectroscopy in truncated dielectric slabs. Phys Rev B 2018;98:205409.
[24] Lagos MJ, Trügler A, Amarasinghe V, et al. Excitation of long-wavelength surface optical vibrational modes in films, cubes and film/cube composite system using an atom-sized electron beam. Microscopy 2018;67:i3–i13.
[25] Hohenester U, Trügler A, Batson PE, et al. Inelastic vibrational bulk and surface losses of swift electrons in ionic nanostructures. Phys Rev B 2018;97:165418.

[26] Krivanek OL, Lovejoy TC, Dellby N, et al. Vibrational spectroscopy in the electron microscope. Nature 2014;514:209–12.
[27] Lagos MJ, Trügler A, Hohenester U, et al. Mapping vibrational surface and bulk modes in a single nanocube. Nature 2017;543:529–32.
[28] Dwyer C, Aoki T, Rez P, et al. Electron-beam mapping of vibrational modes with nanometer spatial resolution. Phys Rev Lett 2016;117:256101.
[29] Hachtel JA, Huang J, Popovs I, et al. Identification of site-specific isotopic labels by vibrational spectroscopy in the electron microscope. Science 2019;363:525–8.
[30] Hage FS, Nicholls RJ, Yates JR, et al. Nanoscale momentum-resolved vibrational spectroscopy. Sci Adv 2018;4:eaar7495.
[31] Govyadinov AA, Konečná A, Chuvilin A, et al. Probing low-energy hyperbolic polaritons in van der Waals crystals with an electron microscope. Nat Commun 2017;8:95.
[32] Idrobo JC, Lupini AR, Feng T, et al. Temperature measurement by a nanoscale electron probe using energy gain and loss spectroscopy. Phys Rev Lett 2018;120:095901.
[33] Hage FS, Kepaptsoglou DM, Ramasse QM, et al. Phonon spectroscopy at atomic resolution. Phys Rev Lett 2019;122:016103.
[34] Konečná A, Neuman T, Aizpurua J, et al. Surface-enhanced molecular electron energy loss spectroscopy. ACS Nano 2018;12:4775–86.
[35] Qi R, Wang R, Li Y, et al. Probing Far-infrared surface phonon polaritons in semiconductor nanostructures at nanoscale. Nano Lett 2019;19:5070–6.
[36] Hachtel JA, Lupini AR, Idrobo JC. Exploring the capabilities of monochromated electron energy loss spectroscopy in the infrared regime. Sci Rep 2018;8:5637.
[37] Hohenester U, Trügler A. MNPBEM–a Matlab toolbox for the simulation of plasmonic nanoparticles. Comput Phys Commun 2012;183:370–81.
[38] Le Gall J, Olivier M, Greffet J-J. Experimental and theoretical study of reflection and coherent thermal emissionby a SiC grating supporting a surface-phonon polariton. Phys Rev B 1997;55:10105–14.
[39] Jain A, Ong SP, Hautier G, et al. Commentary: the Materials Project: a materials genome approach to accelerating materials innovation. APL Mater 2013;1:011002.
[40] Hinuma Y, Pizzi G, Kumagai Y, et al. Band structure diagram paths based on crystallography. Comput Mater Sci 2017;128:140–84.
[41] Allen LJ, Brown HG, Findlay SD, et al. A quantum mechanical exploration of phonon energy-loss spectroscopy using electrons in the aloof beam geometry. Microscopy 2018;67:i24–9.
[42] Ouyang F, Isaacson M. Surface plasmon excitation of objects with arbitrary shape and dielectric constant. Philos Mag B 1989;60:481–92.
[43] Kliewer KL, Fuchs R. Theory of dynamical properties of dielectric surfaces. Adv Chem Phys 1974;27:355–541.
[44] Ashley JC, Emerson LC. Dispersion relations for non-radiative surface plasmons on cylinders. Surf Sci 1974;41:615–8.
[45] Stratton JA. Electromagnetic theory. 1st ed. New York: McGraw-Hill; 1941.
[46] García de Abajo FJ. Optical excitations in electron microscopy. Rev Mod Phys 2010;82:209–75.
[47] Fuchs R, Kliewer KL. Optical modes of vibration in an ionic crystal slab. Phys Rev 1965;140:A2076–88.
[48] Kliewer KL, Fuchs R. Optical modes of vibration in an ionic crystal slab including retardation. I. Nonradiative region. Phys Rev 1966;144:495–503.
[49] Collins SM, Nicoletti O, Rossouw D, et al. Excitation dependent Fano-like interference effects in plasmonic silver nanorods. Phys Rev B 2014;90:155419.
[50] Huang Y, Fang Y, Zhang Z, et al. Nanowire-supported plasmonic waveguide for remote excitation of surface-enhanced Raman scattering. Light Sci Appl 2014;3:e199.
[51] Yalunin SV, Schröder B, Ropers C. Theory of electron energy loss near plasmonic wires, nanorods, and cones. Phys Rev B 2016;93:115408.
[52] Sigle W, Nelayah J, Koch CT, et al. Electron energy losses in Ag nanoholes—from localized surface plasmon resonances to rings of fire. Opt Lett 2009;34:2150–2.

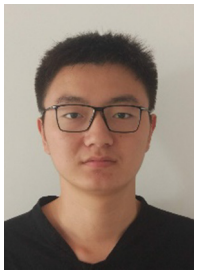

Yuehui Li is a Ph.D. student of Physics at Peking University. His main research is the fast electron nanooptics based on the electron energy loss spectroscopy with both high spatial resolution and high energy resolution, including measurements of phonon, polaritons, and plasmons.

Peng Gao is an Assistant Professor in the International Center for Quantum Materials and a deputy director of Electron Microscopy Laboratory, Peking University. He received his Bachelor degree of Physics from University of Science and Technology of China in 2005 and Ph.D. degree of Physics in the Institute of Physics, Chinese Academy of Sciences in 2010. Before he joined in Peking University at 2015, he worked in University of Michigan, Brookhaven National Laboratory, and The University of Tokyo. His primary research interest is characterization of low dimensional and topological ferroics, electron energy loss spectroscopy, structure and phase transition of energy materials.